Geophysical Journal International

Geophys. J. Int. (2021) **224,** 909–922
Advance Access publication 2020 October 13
GJI Seismology

doi: 10.1093/gji/ggaa488

Shallow slip of blind fault associated with the 2019 M_s 6.0 Changning earthquake in fold-and-thrust belt in salt mines of Southeast Sichuan, China

Ying-Hui Yang,[1] Jyr-Ching Hu,[2] Qiang Chen,[3] Xinglin Lei,[4] Jingjing Zhao,[3] Weile Li,[1] Rui Xu[5] and Chun-Ying Chiu[2]

[1] *State Key Laboratory of Geohazard Prevention and Geoenvironment Protection, Chengdu University of Technology, Chengdu* 610059, *Sichuan, China. E-mail: yangyinghui19@cdut.edu.cn*
[2] *Department of Geosciences, National Taiwan University, Taipei* 10617, *Taiwan*
[3] *Department of Remote Sensing and Geoinformation Engineering, Southwest Jiaotong University, Chengdu* 611756, *Sichuan, China*
[4] *Geological Survey of Japan, AIST, Ibaraki* 305–8567, *Japan*
[5] *Sichuan Earthquake Agency, Chengdu* 610041, *Sichuan, China*

Accepted 2020 October 6. Received 2020 September 9; in original form 2020 February 17

SUMMARY

An earthquake with a magnitude of M_s 6.0 and shallow focal depth of ∼4 km struck the Changning county, Sichuan province, China on 2019 June 17. The hypocentre is located in the fold-and-thrust belt with plentiful shale gas and salt mine resources. One hypothesis is that the shallow fault could be affected by the artificial pressure water injection including the disposal of wastewater, fracking shale gas extraction and salt mining in Changning area. In this study, SAR (Synthetic Aperture Radar) images, historical earthquakes, aftershocks and seismic reflection data were collected to jointly investigate the characteristics of the 2019 Changning earthquake. The source model inferred from the InSAR coseismic deformation observation reveals that the 2019 Changning earthquake is attributed to a blind fault dipping to southwest with dominant thrust and sinistral strike slip. Moreover, a small shallow fault developing within the Changning anticline was triggered by the main shock, which contributed to the surface displacements as observed in the north of the epicentre. The estimated maximum slip of 0.49 m is located at the depth of ∼1.9 km, ∼9 km northwest of the epicentre. The Coulomb failure stress change caused by the previous two large earthquakes, which occurred in the hydraulic fracturing area, suggesting that they have little effect on the initial rupture of the 2019 Changning earthquake. Despite this, they have a positive triggering effect on the fault rupture in the northwest of the seismogenic fault. In addition, the analysis on the relation between the positive Coulomb failure stress change and the aftershocks suggests that the aftershocks may have different motion patterns from the main shock. The analysis also shows the earthquakes occurrence in the seismogenic zone may be affected by the high pore pressure due to the long-term injection of salt mining for more than three decades.

Key words: High-pressure behaviour; Radar interferometry; Joint inversion; Earthquake source observations; Seismicity and tectonics; Dynamics and mechanics of faulting.

1 INTRODUCTION

A devastating earthquake with a magnitude of M_s 6.0 occurred in Changning county, Sichuan province, China on 2019 June 17. The China Earthquake Network Center (CENC) published that the hypocentre (28.34°N, 104.9°E and 19.0 km depth) of the 2019 M_s 6.0 Changning earthquake (CNEQ) is located in ∼50 km southeast of Yibin city. Within 10 hr of the main shock, two strong aftershocks with magnitudes of larger than M_s 5.0 occurred in the northwest of the epicentre (Fig. 1). The severe surface shaking due to the main shock and the large aftershocks caused damages to some roads, bridges and buildings in the seismic zone, resulting in at least 13 people dead and ∼200 people injured (Yi *et al.* 2019).

The Changning earthquake occurred in the interior of Huanan block, and the historical earthquakes were primarily attributed to the kinematic behaviour of the fault-related folding in the study area (Ruan *et al.* 2008; Zhu & He 2014; Sun *et al.* 2017; He *et al.* 2019; Yi *et al.* 2019). However, the GPS observations (Fig. 1) suggest

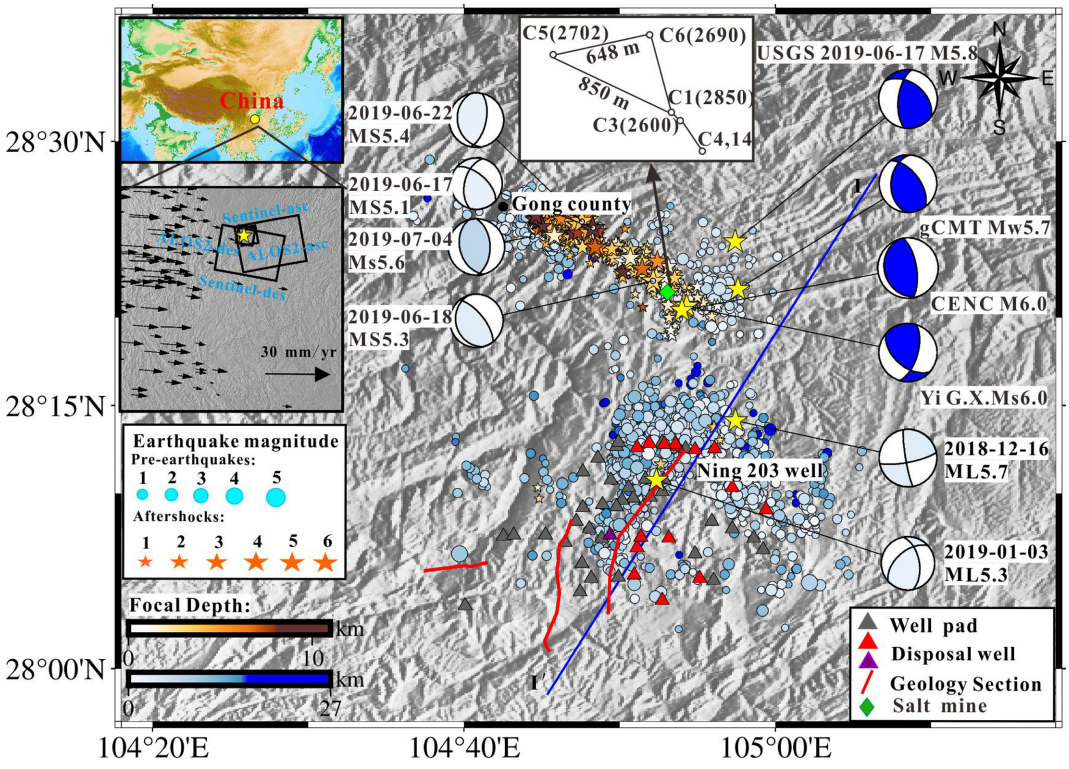

Figure 1. Seismotectonic background of the 2019 Changning earthquake. Blue solid line indicates the surface trace of the seismic reflection section (see Fig. 3); red solid lines indicate the faults. Cool colour-coded solid circles represent the earthquakes occurrence between 2018 December 16 and 2019 May 31. The warm colour-coded solid stars denote the 2019 Changning aftershock sequence. Yellow stars refer to the epicentres of the large earthquakes in the seismic zone, while blue beach balls indicate the source mechanism solutions of the Changning earthquake solved by different institutions. Black arrows indicate the GPS horizontal vectors, and the black rectangles denote the ground coverages of the ALOS-2 and Sentinel-1 images used in this study.

that there is no significant crustal shortening across the seismic zone (Gan *et al.* 2007). In addition, there remains no record of earthquakes with a magnitude that equals to or exceeds M_S 6.0 in this fold-and-thrust belt. Thus, the 2019 M_S 6.0 Changning earthquake is considered to be the largest one in this area up to the present (Yi *et al.* 2019; Lei *et al.* 2019a,b). The sequence of aftershocks following the main shock were distributed along the Changning anticline as part of the South Sichuan thrust-and fold belts (Ruan *et al.* 2008; He *et al.* 2019). It is thus inferred that the faults developing in the Changning anticline are responsible for the 2019 Changning earthquake (Yi *et al.* 2019).

After the main shock, the preliminary fault plane solutions (Table 1) of the 2019 Changning earthquake were estimated by the USGS, CENC and Global CMT project (gCMT) based on the far-field seismic waveform data. It is proposed that a fault plane dipping to northeast should be responsible for the main shock (Fig. 1). However, the preliminary studies conducted by Yi *et al.* (2019) and Lei *et al.* (2019b) using the near-field seismic waveform data indicate that the fault plane dipping to southwest should be the seismogenic fault of the 2019 Changning earthquake (Fig. 1). In addition, the USGS solution shows that the source depth is ∼10 km, which is significantly deeper than ∼3.0 km of the result obtained by Yi *et al.* (2019) and Lei *et al.* (2019b). The aforementioned conflicting solutions presented in the previous studies, indicate the complexity of the fault rupture pattern of the 2019 Changning earthquake. Thus, it is necessary to conduct a detailed investigation of the focal mechanism of the 2019 Changning earthquake on the basis of multidisciplinary observations.

It is worthy to note that the gas and oil exploration and production (Fig. 1) by the hydraulic fracturing technology have been conducted in Changning area and the surrounding towns since 2008 (Lei *et al.* 2013; He *et al.* 2019). As demonstrated in the previous studies, the microseismic events can result directly from hydraulic fracturing (Rutqvist *et al.* 2015; Lei *et al.* 2017, 2019a; Meng *et al.* 2019). For example, hydraulic fracturing is responsible for the large proportion of the unfelt and partly felt earthquakes, which occurred in the shale gas field located in the central part of United States (Ellsworth *et al.* 2015; Walsh & Zoback 2015). Moreover, hydraulic fracturing has also induced many felt earthquakes in western Canada (Farahbod *et al.* 2015; Mahani *et al.* 2017). In Changning shale gas field, the extraction of shale gas by hydraulic fracturing has also resulted in earthquakes with a magnitude over M 5.0 (Lei *et al.* 2013; Zhu & He 2014). Recently, it was suggested by Lei *et al.* (2019a) that the two earthquakes occurred on 2018 December 16 (with magnitude of M_L 5.7) and 2019 January 3 (with magnitude of M_L 5.3) could be attributed to the hydraulic fracturing operation in the Changning shale gas field.

In addition, Changning salt mine is located in proximity to the epicentre of the 2019 Changning earthquake (Lei *et al.* 2019b). The salt extraction is carried out by artificial pressure injection, and the earthquake is suspected to the result from the increase of pore pressure and change of stress loading on the fault due to water injection in salt mine (Bachmann *et al.* 2012; Evans *et al.* 2012; Ellsworth 2013; Rubinstein & Mahani 2015). And the recent study (Sun *et al.* 2017) shows that the increasingly frequent seismic events in the Changning salt mine over the most recent years are associated

Table 1. Estimated fault parameters of the 2019 M_s 6.0 Changning earthquake by different institutions.

Institution/Author	Fault	Strike azimuth (°)	Dip angle (°)	Rake angle (°)
This study	F1	122.3 ± 2.1	27.2 ± 2.6	58.7 ± 1.9
	F2	335.7 ± 1.8	13.1 ± 2.9	148.9 ± 1.7
USGS (2019)	F1	308	45	40
CENC	F1	350	67	93
gCMT	F1	323	57	65
Yi *et al.* (2019)	F1	131	51	36
Lei *et al.* (2019b)	F1	122	53	28

'F1' indicates the seismogenic fault of the 2019 Changning earthquake, and 'F2' is the estimated shallow backthrust fault from InSAR observations.

with the water injection salt mining. Therefore, it is inferred that the water injection salt mining may be also responsible for the occurrence of the 2019 Changning earthquake (Lei *et al.* 2019b).

In this study, we focus on investigating the 2019 Changning earthquake based on the multidisciplinary observations. The ALOS-2 and Sentinel-1 radar satellite images are collected to map the coseismic surface displacements in the seismic zone. The InSAR-derived faulting model and the seismic reflection data are used to identify the seismogenic fault of the 2019 Changning earthquake. The Coulomb failure stress data are calculated to characterize the relationship among the two large earthquakes (occurred on 2018 December 16 with a magnitude of M_L 5.7 and 2019 January 3 with a magnitude of M_L 5.3, respectively), the main shock and aftershocks of the 2019 M_s 6.0 Changning earthquake. Finally, the Coulomb failure stress change due to the main shock and the distribution of the aftershocks is utilized to determine the optimal aftershock mechanism and obtain the best-fitting friction coefficient. Furthermore, the relation between the water injection in salt mine and the 2019 M_s 6.0 Changning earthquake is addressed.

2 MATERIALS AND METHODS

2.1 Data and interpretation

The Synthetic Aperture Radar (SAR) images captured by ALOS-2 and Sentinel-1 satellites (Fig. 1 and Table S1) before and after the main shock of the 2019 Changning event are collected for mapping the coseismic surface displacement fields in the seismic zone. We process the PALSAR-2 images using the GAMMA software with a multilook factor of 18 (azimuth multilook factor) × 8 (range multilook factor) for maintaining the intereferometric coherence (Wegmuller & Werner 1997). And the SRTM-4 Digital Elevation Model (DEM) is used to remove the topographic phase component (Farr *et al.* 2007), and the Snaphu software developed by Chen & Zebker (2002) is adopted to unwrap the interferogram. A bilinear model is constructed based on the high coherence (>0.3) far-field data to simulate and remove the orbital ramp phase. The far-field InSAR data is mainly contributed by the atmospheric delay and other noise signals, thus, we select more than 2000 high coherence (>0.3) far-filed data to assess the accuracy of the observed InSAR deformation (Yang *et al.* 2018b; Yang *et al.* 2019). And the RMS is 1.87 cm of the ALOS-2 ascending, 2.23 cm of the ALOS-2 descending, 1.73 cm of the Sentinel-1 ascending and 1.49 cm of the Sentinel-1 descending data. Above-mentioned low RMS suggests that both the derived ALOS-2 and the Sentinel-1 InSAR data are reliable enough to reveal the coseismic surface motion of the 2019 Changning earthquake.

The Fig. 2 shows the coseismic InSAR (Interferometric Synthetic Aperture Radar) surface displacement fields extracted from the ALOS-2 and Sentinel-1 SAR images. It can be found from Fig. 2 that there are significant coseismic surface displacements in the northwest of the epicentre, which indicates that the coseismic fault rupture extends only from the hypocentre towards the northwest on the fault plane (Fig. 2). In addition, there is no sharp surface deformation discovered in the seismic zone, suggesting that the coseismic fault rupture should have not propagated to the ground surface (Figs 2a and c).

As shown in Figs 2(e)–(h), the near-fault interferograms (the masked areas) associated with the main shock cannot be well obtained from the ascending and descending track of Sentinel-1 images. It suggests that the 2019 Changning earthquake has caused the significant surface displacement in the near-fault. This is supposed to result from the significant fault slip occurrence in the shallow crust. The ALOS-2 satellite has a longer radar wavelength (24.26 cm) than that (5.55 cm) of Sentinel-1 satellite, which makes the ALOS-2 InSAR interferograms have better interferometric coherence in the vegetation covering area due to the strong penetrability of long wavelength radar. In addition, longer radar wavelength provides a stronger detecting ability of the large deformation gradient (Hanssen 2001; Yang *et al.* 2018c). Therefore, the near-fault surface deformation has been well extracted from both the ascending and descending ALOS-2 images, which would provide a great help for the understanding of the mechanism of the 2019 Changning earthquake.

The studies carried out by Yi *et al.* (2019) and Lei *et al.* (2019b) proposed that the NW-SE striking and SW-dipping seismogenic fault (the blue dashed line in Fig. 2) is the primary source fault of the 2019 CNEQ based on the near-field seismic data. However, there is a significantly negative deformation area (within the red dashed ellipse) in the southeast of the footwall of the seismogenic fault (Figs 2c and g). In addition, the LOS deformation distribution (Fig. 3) along the selected profile SS' (the black solid line in Fig. 2) shows that there is significant deformation in the triangle zone of the Changning anticline, which implies that a shallow backthrust in a triangle zone could be triggered by the main event. Thus, it is hypothesized that the rupture of a small fault within the Changning anticline is partly responsible for the negative InSAR deformation data as observed within the red dashed ellipse (Fig. 2). However, the multilayer overlying fault-bend folds at different depths (Fig. 3) make it difficult to distinguish which one has been triggered by the main shock.

2.2 Faulting model estimated by InSAR observations

To obtain the detailed coseismic fault rupture model of the 2019 Changning event, the observed InSAR surface displacement fields are used to estimate the fault geometry and slip distribution. Firstly, the unreliable InSAR data with interferometric coherence less than

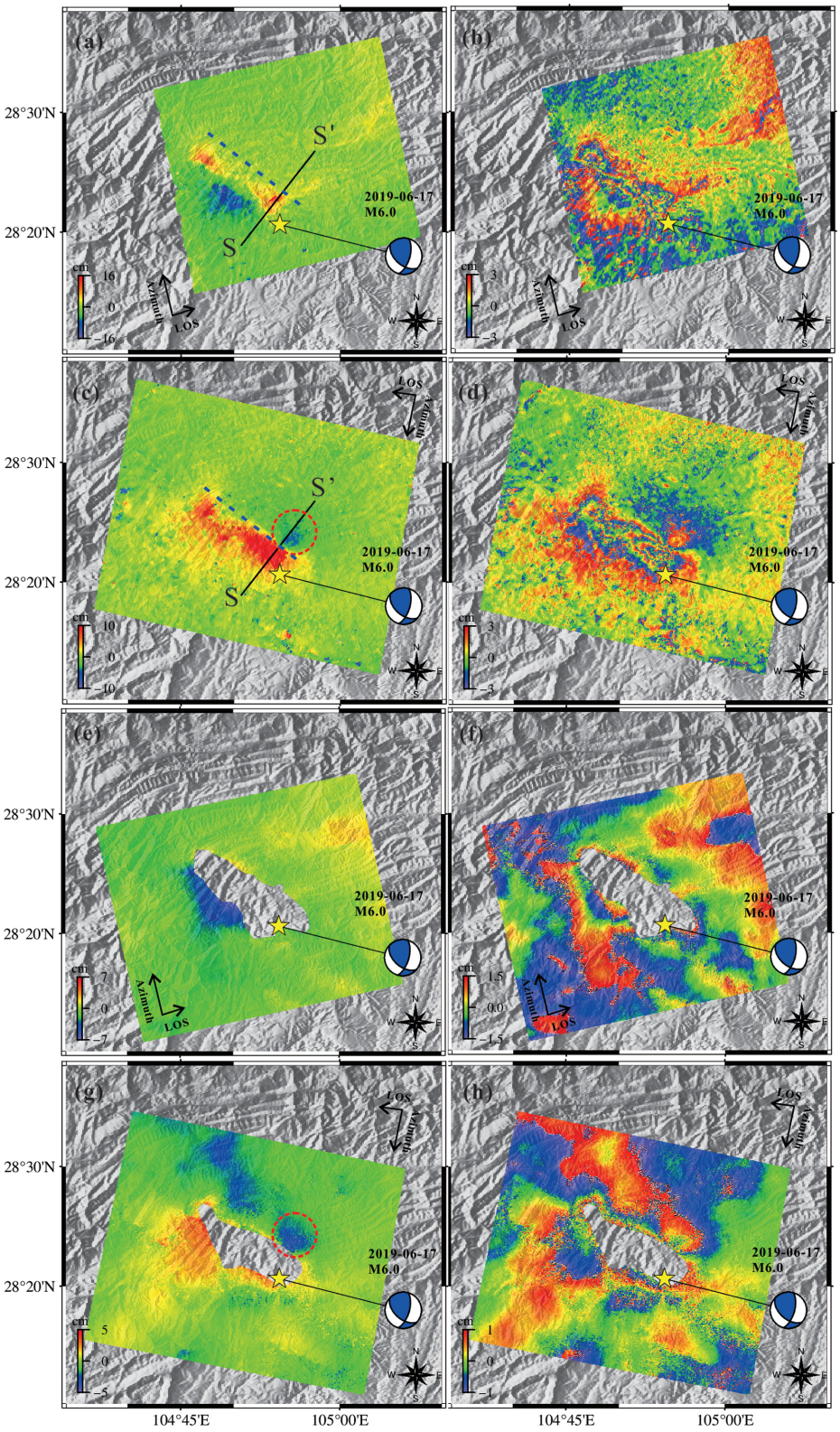

Figure 2. InSAR coseismic deformation field of the 2019 Changning earthquake derived from ALOS-2 and Sentinel-1 radar images. (a) ALOS-2 ascending, (c) ALOS-2 descending, (e) Sentinel-1 ascending, (g) Sentinel-1 descending track InSAR deformation field, and (b), (d), (f) and (h) show the wrapped InSAR observations of ALOS-2 and Sentinel-1. Yellow star indicates the epicentre of the main shock. Red dashed ellipse denotes the significant negative deformation area identified from the descending track InSAR displacement field, blue dashed line suggests the deduced surface trace of the seismogenic fault of the 2019 Changning event, and the black solid line denotes the surface trace of the deformation section shown in Fig. 3.

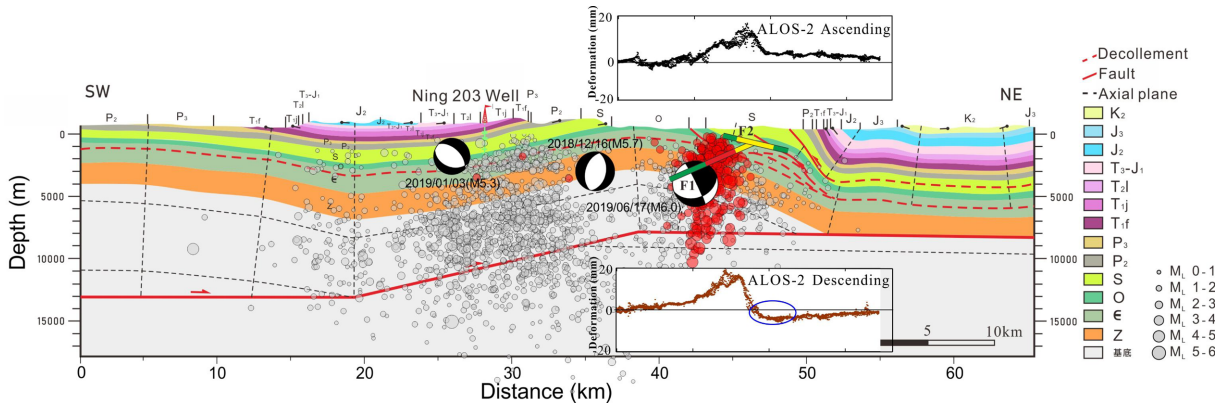

Figure 3. Geological cross section II' shown in Fig. 1 (modified after He *et al.* 2019). Grey dots indicate the background earthquakes occurring around the seismic zone, while the red dots denote the relocated aftershocks provided by Yi *et al.* (2019). Weighted lines coloured by green (insignificant slip segment), red (peak slip segment) and yellow (significant slip segment) indicate the inferred coseismic fault of the 2019 Changning earthquake. F1 represents the inferred seismogenic fault by InSAR-derived surface deformation, while F2 refers to the triggered shallow backthrust fault within the Changning anticline.

0.3 are removed from the original observations (Fig. 2). Then, we down-sample the remained InSAR deformation data using the quadtree method. And total 1843 Sentinel-1 data and 2539 ALOS-2 observations are preserved for the estimation of the coseismic faulting model.

A NW-striking and SW-dipping fault is firstly constructed to describe the seismogenic fault of the 2019 Changning earthquake. And the fault is composed by three individual segments (with different dip angles) along the downdip direction due to the possibility that a listric fault rupture or a flat-ramp structure is responsible for the 2019 Changning earthquake. However, the inversion result shows that the dip angle difference between the first (26.8°) and second (29.1°) segments is not significant, especially, the high-slip area is mainly located on the first segment (Fig. S1). The dip angle of the third segment is 39.5°, which is significantly larger than those of the first two segments. However, it can be found from Fig. S1 that there is no significant slip occurred on the third segment. In addition, the high-slip area of the two fault models (Fig. S1 and Fig. 4) has a good consistency in both the magnitude and the slip distribution. And the slight difference between the two slip models should be caused by the insignificant discrepancy of the fault dip angle (27.2° of the best-fitting fault model and 26.8° of the curved fault model) of the high-slip area. Therefore, it is believed that a planar fault with a uniform dip angle along the downdip direction should be the seismogenic fault of the 2019 Channing earthquake.

Furthermore, a planar fault with a dip angle of 50° also has been constructed to describe the seismogenic fault of the 2019 Changning earthquake based on the previous studies (Yi *et al.* 2019; Lei *et al.* 2019b). Fig. S3 shows that the estimated faulting model has a similar slip distribution, but a larger slip magnitude compared with the curved (Fig. S1) and the best-fitting faulting model (Fig. 4). And above-mentioned difference could be caused by the remarkable discrepancy between the fault dip angles (27.2° of the best-fitting fault model, 26.8° of the curved fault model and 50° for the fixed dip angle fault model) of the high-slip area.

Furthermore, the InSAR deformation residual (Figs S4b and d) shows that there are significant residual fringes on the hanging wall of seismogenic fault. However, these significant deformation residual on the hanging wall has not been found in the results (Figs S2 and 5) of the curved (Fig. S1) and best-fitting faulting model (Fig. 4). Therefore, it is hypothesized that the dip angle of 50° may be not the most appropriate choice for the 2019 Changning earthquake.

In addition, it is worthy to note that both the Figs S2 and S4 show that the single main fault is failed to explain the significant deformation zone (within the red dashed ellipses in the Figs S2(d), S2(h) and black dashed ellipse in the Fig. S4d) on the foot wall of seismogenic fault. And it is hypothesized that the shallow NE-dipping backthrust fault within the Changning anticline (Fig. 3) may has been triggered by the rupture of the seismogenic fault, and may contribute to the observed surface deformation on the foot wall.

Therefore, a SW-dipping fault and a NE-dipping fault are respectively constructed, to represent the main fault (F1 in Fig. 3) and the inferred backthrust fault (F2 in Fig. 3) within the Changning anticline. And the searching bounds of the strike angle, dip angle and rake angle of the main fault are set as [80°, 150°], [2°, 89°] and [−180°, 180°] based on the focal mechanism obtained from the near-field seismic data (Yi *et al.* 2019). The searching range of the backthrust fault parameters are respectively set as [270°, 360°] for the strike angle, [2°, 89°] for the dip angle and [−180°, 180°] for the rake angle. And the starting values of the main fault is set as strike angle of 131°, dip angle of 51°and rake angle of 36°based on the solution derived from seismic data (Yi *et al.* 2019). The starting values of the backthrust fault are randomly generated within the searching range.

Here, the proposed method of faulting model estimated by geodetic data by Yang *et al.* (2018a,b,c) is applied to infer the best-fitting faulting model of the 2019 Changning earthquake. And the crust is assumed to be homogeneous and isotropic elastic medium with a shear modulus of 30 GPa and Poisson's ratio of 0.25 (Okada 1985,1992). The two faults are firstly divided using the size of 3 km × 3 km to get the best-fitting fault geometry parameters. And the best-fitting fault geometry parameters and the relative errors could be found in Table 1. Then, we redivide the two faults using a small size of 0.5 km × 0.5 km to infer the fault slip distribution (Fig. 4) based on the InSAR observations. The sufficient near-field and far-field InSAR deformations make it possible to well constrain the fault slips both in the shallow and deep crust. Moreover, a checkboard test (Fig. S5) is performed to assess the resolution of the derived faulting model. It can be found from Fig. S5 that most of the simulated fault slip have been recovered both in magnitude and

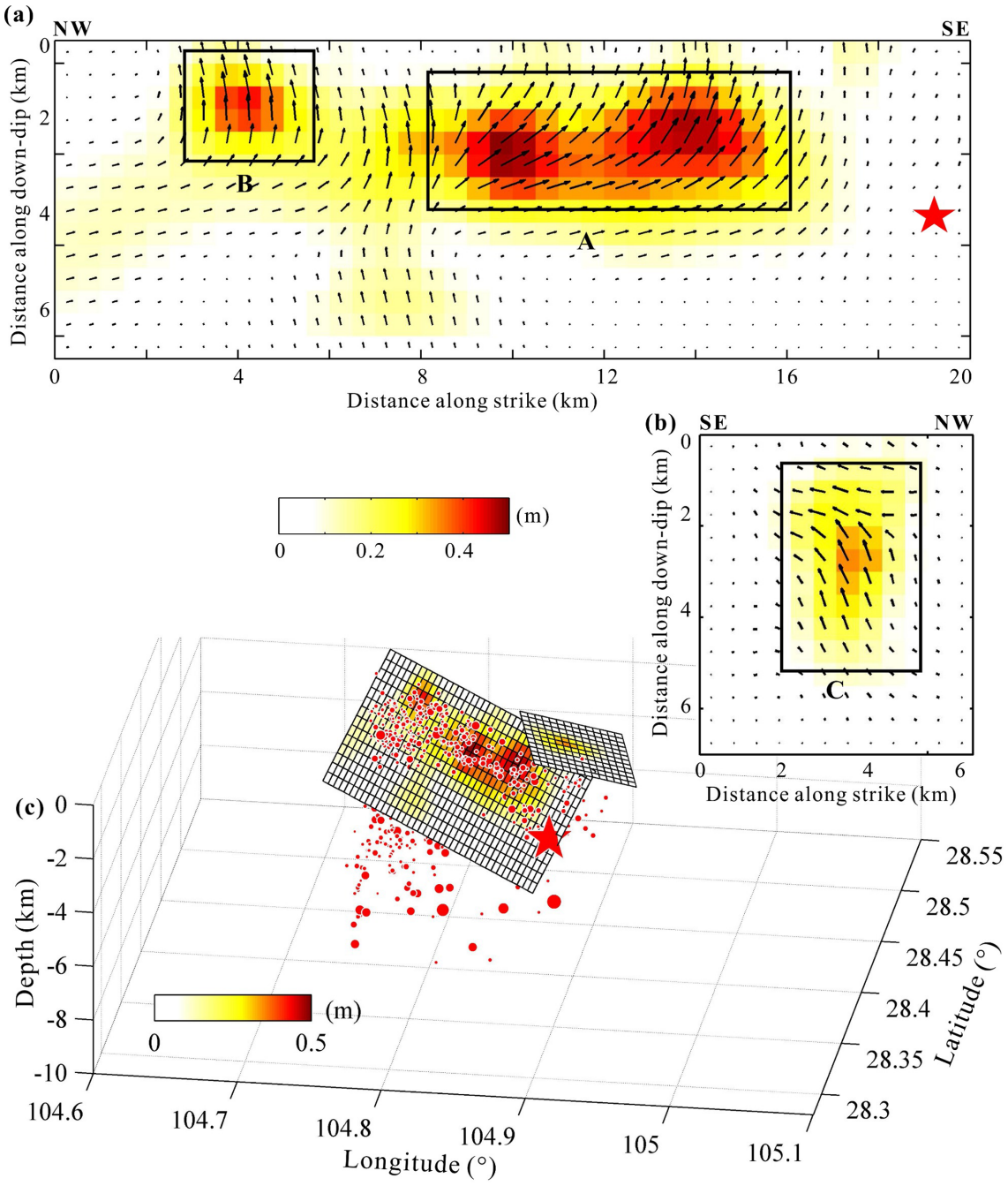

Figure 4. Inferred faulting model of the 2019 CNEQ from the ALOS-2 and Sentinel-1 InSAR observations. Red dots indicate the aftershock sequence of the main shock, red star denotes the hypocentre of the main shock and three black rectangles represent the high-slip areas on the two seismogenic faults.

shape, especially the fault slip within the shallow crust. In addition, the significant slip areas (see Fig. 4) on both the F1 and F2 have a high slip resolutions. It suggests that both the number of the selected InSAR observation and the patch size of the fault are appropriate for revealing the fault motion of the 2019 Changning earthquake.

2.3 Calculation of the coulomb failure stress

The Coulomb failure stress (CFS) has been widely used to reveal the relation between the aftershocks and coseismic fault rupture (Toda *et al.* 2012). The CFS change could be calculated based on the eq. (1).

$$\Delta \mathrm{CFS} = \Delta\tau + \mu \cdot (\Delta\sigma + \Delta P), \tag{1}$$

where ΔCFS indicates the CFS change on a receiver fault with given parameters including strike angle, dip angle and rake angle. $\Delta\tau$ and $\Delta\sigma$ denote the shear stress and normal stress change, which could be calculated based on the coseismic faulting model and the fault receiver parameters (Okada 1992). ΔP is the pore pressure change that is difficult to collect in the most of the time, therefore, it is not considered in this study. μ is the friction coefficient that varies from 0.1 to 0.8 due to different characters of the rock, faulting and stress (Hsu *et al.* 2010; Toda *et al.* 2012).

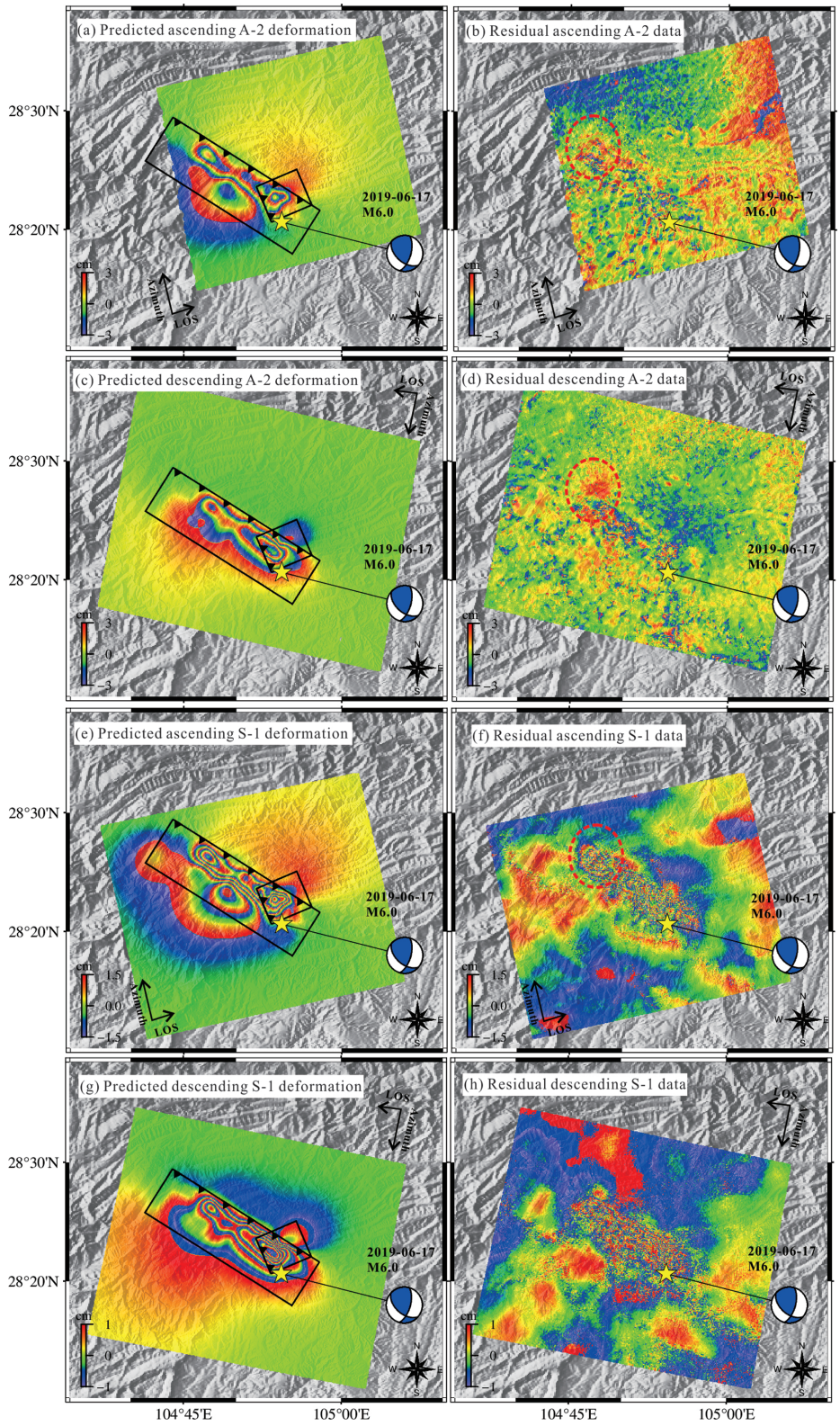

Figure 5. Predicted InSAR deformation (a, c, e and g) from the estimated faulting model of the 2019 CNEQ, and the residual component (b, d, f and h) between the observed and predicted data. Two black rectangles indicate the surface projections of the two estimated seismogenic faults of this event, yellow star denotes the epicentre of the main shock, and red dashed ellipse refers to the significant deformation residual area. 'A-2' indicates the ALOS-2 satellite and 'S-1' denotes the Sentinel-1 satellite.

3 RESULTS

The optimal faulting model shows that the main fault (marked by F1 in Figs 3 and 4) dips to southwest and the coseismic rupture is controlled by predominant reverse and slight sinistral strike-slip motion. It is worthy to note that the estimated main fault could be a blind thrust fault breaks through the forelimb of Changning anticline, and it is not interpreted from the geological cross section (Fig. 3). The location of geological cross section is about 10 km west of the epicentre the main shock, thus the estimated major fault could not be well constrained due to lack of available high-resolution seismic profiles and well data.

In addition, a small backthrust fault (marked by F2 in Figs 3 and 4) dipping to northeast within the Changning anticline has also ruptured in the 2019 main shock. The fault rupture on the F2 is controlled by the predominant reverse motion with the slight dextral slip. The estimated geodetic magnitude of the 2019 CNEQ is M_w 5.86, which is consistent with the moment magnitude solved by USGS. Figs 3 and 4 show that more than 97 per cent seismic moment is released at the depths of 1.0–2.5 km, and there is no significant slip found below 3.0 km. In addition, the inferred fault slip is concentrated in northwest of the epicentre, which suggests that the coseismic fault rupture extends only from the epicentre to the northwest along the seismogenic fault.

A slip asperity near the hypocentre marked by 'A' can be found in the Fig. 4, which is located at the along strike distance of 8–16 km and along downdip distance of 1–4 km, indicating that the fault rupture has not propagated to the ground surface in this area. The maximum slip magnitude of the Changning earthquake is 0.49 m, which is located at the depth of ∼1.9 and ∼9 km northwest of the epicentre. The average slip is ∼0.4 m in the region 'A', and more than 92 per cent seismic moment of the main shock is released in this area. Another slip asperity marked by 'B' is located at the along-strike distance of 3–5 km and along down-dip distance of 0.5–2.5 km. The fault slip pattern in the area 'B' is different from that in the area 'A', and it is dominated by the reverse motion with a quite slight dextral slip. Moreover, it is worth noting that many aftershocks occurred on the northwest of the seismogenic fault (Figs 1 and 4), implying the possibility that the detected faulting is caused by the dense aftershocks on this segment.

There is a small slip asperity marked by 'C' in the centre of the F2. The fault slip in the area of 'C' is concentrated at the depths of 0.5–0.9 km beneath the ground surface, which leads to the significant surface motion within the red ellipse in Fig. 2. Moreover, Fig. S6 shows that the seismogenic fault (F1) rupture increases the CFS in the high-slip area of F2, indicating that the small backthrust fault within the Changning anticline could be triggered by the rupture of the main fault of the 2019 CNEQ. It is worthy to note that the inferred fault motion on the F2 also may be caused by the creep and aseismic slip, which have been found in the fault-related fold belt after a moderate earthquake in Japan and Taiwan (Nishimura *et al.* 2008; Huang *et al.* 2016; Le Béon *et al.* 2017). However, it is difficult to distinguish the coseismic rupture and creep, aseismic slip due to the low temporal resolution of the InSAR observation in this event. Collecting the high temporal resolution GPS and the InSAR data could provide a great help for distinguishing these motions.

Fig. 5 shows the InSAR deformation fields predicted from the estimated faulting model (Fig. 4). It is found that the predicted InSAR fringes (Fig. 5) are consistent with the observations shown in Fig. 2. Additionally, more than 94.4 per cent of the ALOS-2 ascending, 95.7 per cent of the ALOS-2 descending data, 97.1 per cent of the Sentinel-1 ascending data and 98.3 per cent of the Sentinel-1 descending data could be explained by the inferred faulting model. Moreover, it can be found from Figs 5(b) and (d) that there is no significant residual signal in the near-fault area, which suggests that the predicted InSAR deformation has a good consistency with the observations (Fig. 2). And the far-filed residual signals should be mainly contributed by the atmospheric delay phase. Figs 5(f) and (h) show that the significant residuals are mainly located in the near-fault area where the Sentinel-1 InSAR observations are unreliable due to low interferometric coherence. The slight residual in the northwest of the seismogenic fault (Figs 5b and d) could be attributed to the deformation resulting from a combination effect of the aftershocks, the triggered landslides and the atmospheric delay noise (Yang *et al.* 2018a).

4 DISCUSSION

4.1 A gentle dipping seismogenic fault in fold-and-thrust belt

Table 1 shows that the estimated strike angle of the seismogenic fault is 122.3°, which is consistent with the results of the previous studies (Yi *et al.* 2019; Lei *et al.* 2019b). However, the best-fitting dip angle of the seismogenic fault is 27.2°, which is smaller than ∼50° as proposed by Yi *et al.* (2019) and Lei *et al.* (2019b). It is believed that above mentioned discrepancy should be attributed to the different observations, crust velocity models and inversion methods (Weston *et al.* 2012). In addition, it should be noted that the seismic site is very sparse in the southeastern of the epicentre of the 2019 Changning earthquake (Yi *et al.* 2019; Lei *et al.* 2019b). It will reduce the reliability of the solution. Moreover, the lack of 3D crust velocity model could significantly increase the uncertainty of the faulting parameters solved by the seismic data of the 2019 Changning earthquake (Weston *et al.* 2012). Furthermore, it is found that the inferred small fault F2 shows an excellent consistency with the existing faults within the Changning anticline (Fig. 3), which means that the estimated fault geometry parameters should be reliable for this study. Thus, it is believed that the estimated dip angle of the seismogenic fault should also be reliable for this study.

However, it is worthy to note that above InSAR-derived faulting model may be not the best one due to the assumption of a homogeneous and isotropic elastic medium. The crust structure is highly complex in the fold and thrust-belt in general (McQuarrie 2004; Yue *et al.* 2005; Kato *et al.* 2009). The previous studies reported that the assumption of a homogeneous and isotropic elastic medium may be too simple to represent the real crust structure of the fold-and-thrust belt (Cattin *et al.* 1999; Weston *et al.* 2012). According to the parametric study in Young's modulus ratio between the upper layer and the underlying half-space (Cattin *et al.* 1999), the coseismic horizontal displacement vary by more than 40 per cent. In addition, the sensitivity of normalized displacements to the low-rigidity layer is almost the same for fault dip ranging from 20° to 60°. Therefore, a fine heterogeneous crust model would provide a great help for the improvement of the faulting model of the 2019 Changning earthquake for further study.

4.2 Triggering effect by two large earthquakes occurrence in the hydraulic fracturing area

Fig. S7(a) shows the distribution of the seismic events with a magnitude larger than M 3.0 that occurred in the seismic zone between

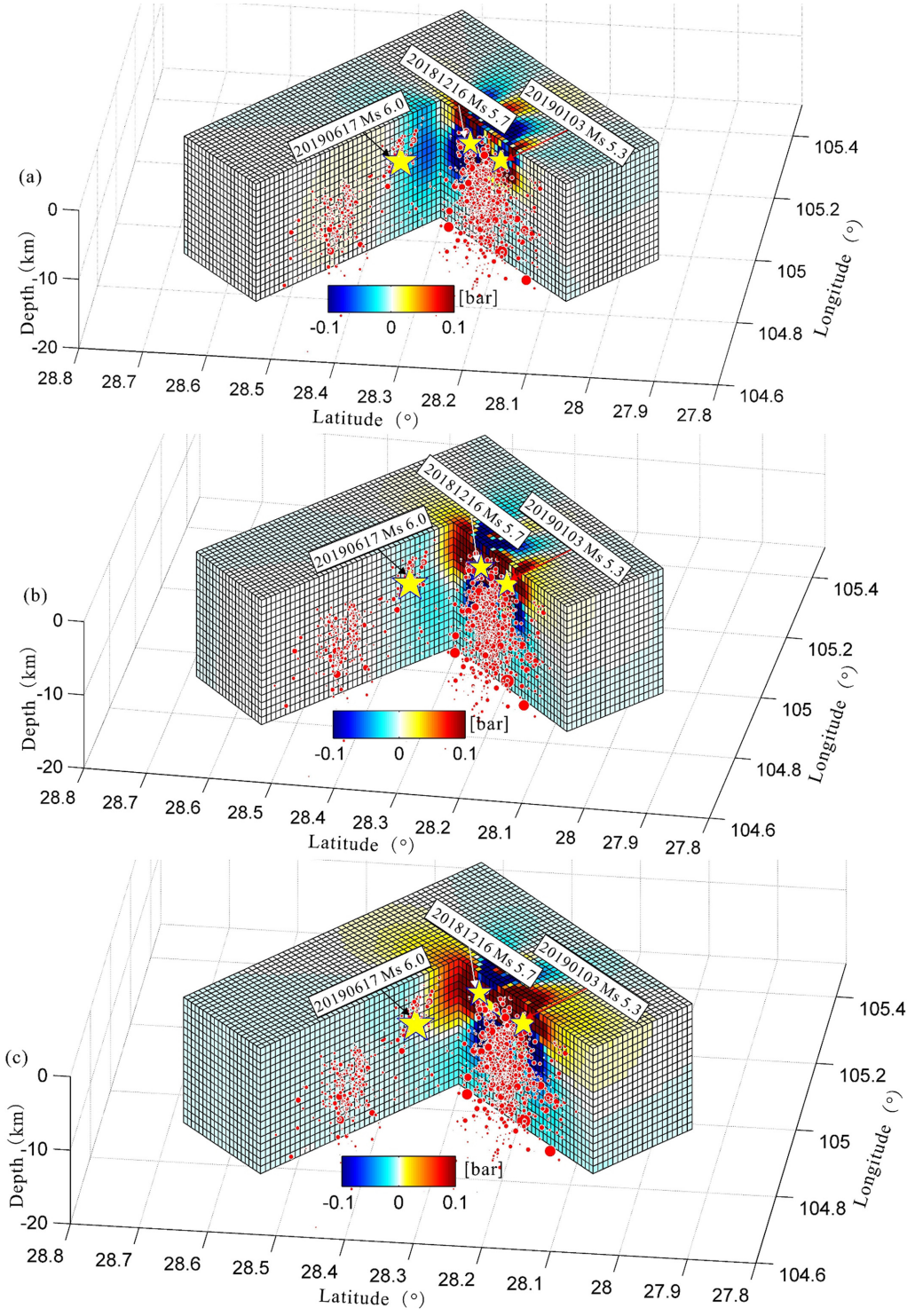

Figure 6. Coulomb failure stress changes due to the two large earthquakes that occurred in the seismic zone. Parameters for receiver fault geometry are the same as the main faulting model (strike angle of 122.3°, dip angle of 27.2°) of the 2019 CNEQ. Rake angle of receiver fault is set to 0° for (a), 45° for (b) and 90° for (c). Red dots indicate the background seismic events that occurred between 20187 December 16 and 2019 May 31, and yellow stars denote the epicentres of the three earthquakes.

2009 January 1 and 2019 May 31. It is found that many of the earthquakes occurred in the seismic zone and the hydraulic fracturing area (Fig. S7a). Moreover, two large earthquakes with a magnitude of M_L 5.7 (2018 December 16) and M_L 5.3 (2019 January 3) occurred in the hydraulic fracturing area (southeast of the seismic zone) within half a year. In order to quantitatively assess the influence of the two large earthquakes on the occurrence of the 2019 Changning earthquake, the Coulomb failure stress change in the seismic zone of CNEQ caused by the two large events is calculated, and the receiver fault geometry parameters are the same as the main

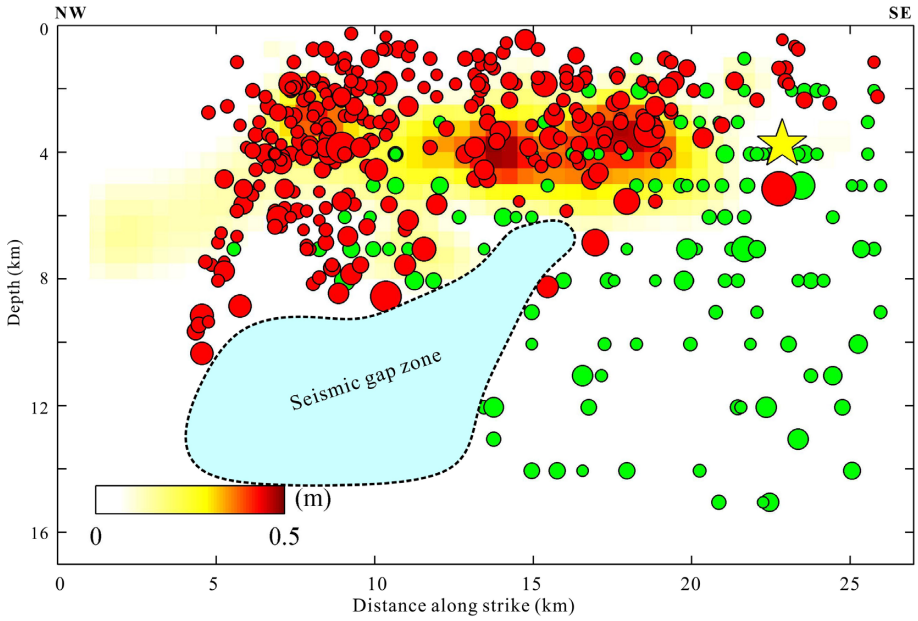

Figure 7. Distribution of the aftershocks and the background seismic events along the seismogenic fault (F1-fault). Red dots indicate the aftershock sequences of the 2019 Changning earthquake, green dots denote the background earthquakes, yellow star indicates the hypocentre of this event, and the light blue area represents the detected seismic gap zone.

faulting model (strike angle of 122.3°, dip angle of 27.2°) of the 2019 Changning event.

We collect the focal mechanism solutions (Table S2) of the two large earthquakes based on the study by Lei *et al.* (2019a). And the empirical relationship between the seismic moment magnitude and fault rupture size: $M_w = \log_{10} A – 2.0$ (A represents the fault rupture size) is used to estimate the fault area (Leonard 2010). The average of the fault slip magnitude is calculated by $M_o = GuA$ and M_o is the seismic moment, G indicates the shear modulus of the elastic medium and u is the average slip on the fault. Then, we can calculate the Coulomb failure stress change based on the Okada elastic dislocation model (Okada 1992; Yang *et al.* 2018a; Lei *et al.* 2019a).

Fig. 6 shows the predicted CFS change with different receiver rake angles. It can be found that the derived CFS changes in the northwest of the hypocentre are positive when the receiver rake angle is less than 90° (Figs 6a and b). It suggests that the past two large earthquakes may have a positive triggering effect on the rupture in the most area of the seismogenic fault. However, it is worth noting that the CFS change is negative at the hypocentre when the receiver rake angle is less than 90°, indicating that the two large earthquakes have little impact on the initial rupture in the hypocentre of the 2019 CNEQ.

Fig. 1 shows that there are plenty of shallow aftershocks (focal depth less than 8 km) occurrence in the northwest of the seismogenic fault after the 2019 CNEQ. Furthermore, Fig. 6 shows that a large number of small earthquakes occurred between 2018 December 16 and 2019 May 31 in this area following the previous two large events (occurred on 2018 December 16 and 2019 January 3, respectively). Besides, there are many exploratory wells distributed across this area, but no shale gas and/or salt extraction operation have been executed over the past years. However, it is worthy to note that this dense earthquake area in the northwest of the seismogenic fault is only ∼14 km from the salt mining area. And the study by Zhu & He (2014) has shown that a lot of earthquakes have been triggered by the water injection of salt mining in this area. Therefore, it is hypothesized that the water injection of salt mining could also contribute to the earthquake occurrence in the northwest of the salt mining area.

In addition, the two large events have a positive triggering effect on the occurrence of the earthquakes in this area (Fig. 6). However, the CFS change caused by the two large earthquakes is ∼0.02 bar, which is too small to trigger the earthquake. Therefore, it is hypothesized that the high-frequency earthquakes in the northwest of the hypocentre of the Changning earthquake could be jointly caused by the two large earthquakes occurred in the hydraulic fracturing area and the water injection of the salt mining. The detailed water injection of salt mining and geology data would help us understand more of the relation between the earthquakes occurred in the northwest of hypocentre and salt mining.

4.3 Aftershocks and historical earthquakes distribution

We collect the historical earthquakes occurred in the seismic zone from the study by Lei *et al.* (2019b) and relocated aftershocks of the 2019 Changning earthquake from the study by Yi *et al.* (2019). Fig. S7(b) shows the distribution of the aftershocks with a magnitude larger than M 2.0 that occurred in the seismic zone. It is obvious that the aftershocks have a high spatial consistence with the coseismic fault slip of the 2019 Changning earthquake. Furthermore, the historical earthquakes with distances less than 3.0 km from the seismogenic fault and magnitudes larger than M 2.0, the aftershocks and coseismic fault slip are projected onto the vertical plane along the trace of the seismogenic fault [the top edge of the main fault (F1) shown in Figs 5 and S7], as shown in Fig. 7.

It is noticed that the historical earthquakes (green dots) mainly occurred at the along-strike distances of 8–25 km and at depths of 3–16 km. The shallow fault with significant coseismic fault rupture is a remarkable seismic deficit zone before the 2019 CNEQ. Furthermore, the aftershocks distribution is complementary to the historical earthquakes, and the most aftershocks occurred in the

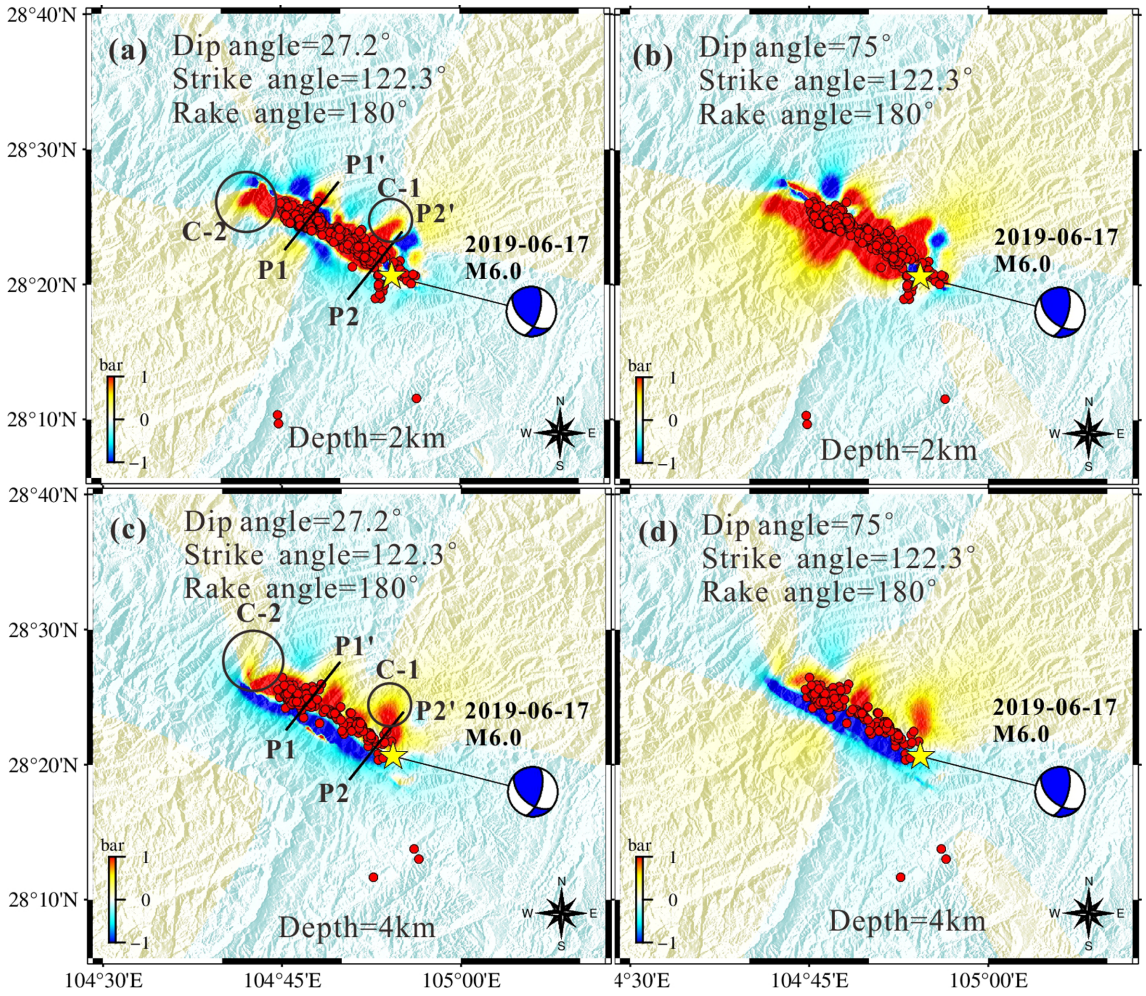

Figure 8. Coulomb failure stress change at aftershocks cluster depths of 2 and 4 km caused by the faulting of the 2019 Changning earthquake. CFS change at 2 km depth with the receiver fault strike angle of 122.3°, rake angle of 180° and different dip angles of 27.2° for (a), 75° for (b). CFS change at 4 km depth with the receiver fault strike angle of 122.3°, rake angle of 180° and different dip angles of 27.2° for (c), 75° for (d). Two black ellipses marked by 'C-1' and 'C-2' denote the identified significant CFS change areas with few aftershocks. Two black solid lines indicate the surface traces of the two CFS sections shown in Fig. 9.

previous seismic gap zone, especially in the northwest of the seismogenic fault. It suggests that the historical earthquakes, coseismic fault slip and aftershocks may have caused complete rupture of the seismogenic fault. However, the magnitude of the Changning event is only M_s 6.0, and no surface rupture is observed. Considering that the seismic zone is located in an active compressional zone, it is necessary to take care of more serious future seismic hazards with magnitudes larger than M_s 6.0 in this area. Furthermore, it is also noticed that few of historical earthquakes and aftershocks can be found in the recognized seismic gap zone (Fig. 7), which may indicate a high potential of future seismic event.

4.4 Coulomb failure stress change and aftershocks

In order to further investigate the correlation between the main shock and the aftershocks, the CFS change (Figs 8, S8 and S9) at the aftershock concentration depths of 2 and 4 km (more than 80 per cent aftershocks occurred at depths 1–5 km) is calculated based on different receiver fault dip and rake angles. For the depths of 2 and 4 km, we calculate the CFS change based on two groups of fault receiver parameters, the first group shares the similar parameters with the main fault of 122.3° for the strike angle, 27.2° for the dip angle, 0° (Figs S8a and S9a), 45° (Figs S8b and S9b), 90° (Figs S8c and S9c), 135° (Figs S8d and S9d) and 180° (Figs 8a and c) for the rake angle. And the second group (Figs S8e–h, S9e–h and Figs 8b and d) shares the similar fault receiver parameters with the first group, except for a high dip angle of 75°. In addition, the friction coefficient is set as 0.4 due to that it is difficult to assign the best value, thus, the middle value of the possible range is chosen.

Figs 8 and S8 demonstrate that more than 70 per cent aftershocks occurrence in the area with positive CFS change when the receiver fault rake angle is excess of 135° for both the low dip angle (27.2°, same as the inferred dip angle of the main shock) and high one (75°) receiver fault dip angles at the depth of 2 km. However, it is found that the aftershocks and positive CFS change exhibit a good spatial consistency only in the case of low dip angle and large (180°) rake angle at the depth of 4 km (Figs 8 and S9). In addition, the relation between the aftershocks and CFS change (Figs S10 and S11) due to faulting model with a uniform dip angle of 50° (Fig. S3) also shows that the larger rake angle would cause a higher spatial consistency of the aftershocks and positive CFS change, especially at the depth of 2 km (Fig. S10e). Thus, we hypothesized that the faulting model

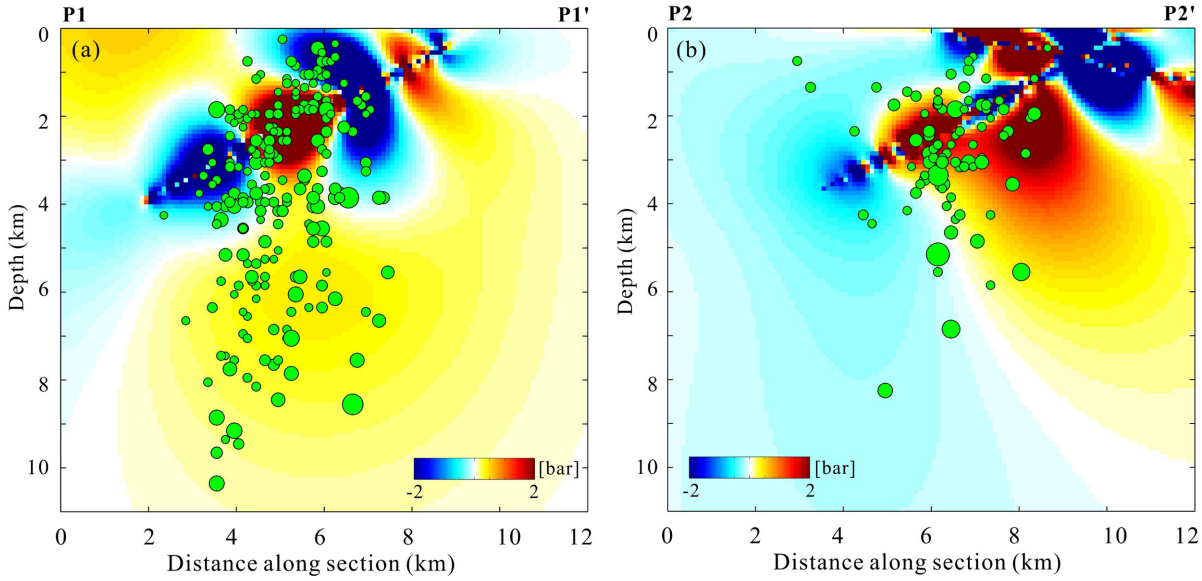

Figure 9. CFS change in the two selected sections of P1–P1′ (a) and P2–P2′ (b), and the location of the two sections are shown in Fig. 8. Receiver fault parameters are set as strike angle of 122.3°, dip angle of 27.2° and rake angle of 180° (optimal rake angle detected from Figs S3 and S4). Green dots indicate the aftershock sequences of the 2019 CNEQ.

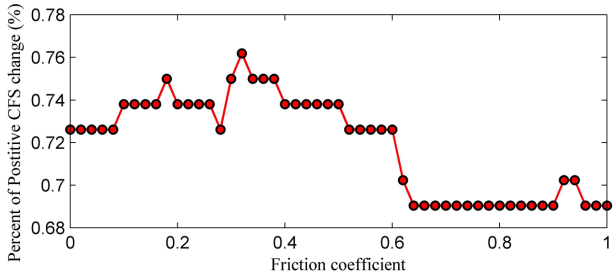

Figure 10. Trade-off relation between the percentage of positive CFS change and friction coefficient for the sections P2–P2′ in the salt mine area.

of most aftershocks could be characterized by a low dip angle and significant strike slip component. Moreover, the previous studies have proposed the possibility that the strike slip component of the earthquake results from the high pore pressure in the water injection area (Sun *et al.* 2017; Liu & Zahradnik 2019). In addition, the CFS change is larger than 1.0 bar in the northeast (marked by 'C-1') and northwest (marked by 'C-2') of the seismogenic fault (Fig. 8). However, few aftershocks have occurred in these areas, which indicates potential but not certain future seismic event in the areas of 'C-1' and 'C-2'.

Furthermore, we calculate the CFS change in the two selected sections (the black solid lines in Fig. 8) with receiver fault strike angle of 122.3°, dip angle of 27.2° and rake angle of 180°. As shown in Fig. 9, ∼65.3 and ∼75.2 per cent of the aftershocks are located in the areas with positive CFS change for sections P1–P1′ and P2–P2′, respectively. It indicates that the aftershocks in the southeast of the seismogenic fault have a higher tendency to occur on a fault characterized by low dip angle and high rake angle than in the northwest. In addition, Fig. 4 indicates that the rake angle of most fault patches is less than 90° for the main shock. Therefore, it is suggested that the most aftershocks may have different motion patterns from the main shock. The above-mentioned inconsistency between the main shock and the aftershock sequences should result from the complex geological structure in the seismic zone (He *et al.* 2019; Yi *et al.* 2019).

Previous studies show that the friction coefficient could be used to reveal the characteristics of the stress on the fault (Hsu *et al.* 2010; Toda *et al.* 2012). Here, we firstly calculate the shear stress and normal stress change of the section P2–P2′ (Fig. 8) due to the coseismic fault slip based on the Okada elastic dislocation model (Okada 1992). Then, we calculate the CFS change using the linear varying friction coefficients within the range of 0.0–1.0 based on the equation 1 (Yang *et al.* 2018a). And the trade-off relation between the percentage of positive CFS change and friction coefficient is shown in Fig. 10.

It can be found from Fig. 10 that the maximum percentage of the positive CFS change is ∼76 per cent at the friction coefficient of 0.36. The low friction coefficient indicates significant cumulative slip and/or high pore pressure on the fault (Hsu *et al.* 2010; Toda *et al.* 2012; Yang *et al.* 2018a,c). Moreover, the study performed by Lei *et al.* (2019b) proposed that the overpressurized water can flow out along the fault within the Changning anticline and play an important role in weakening the pre-existing fault. It can facilitate the reactivation of a pre-existing fault due to the accumulation of shear stress and increase the possibility of the earthquake occurrence in the salt mine area. Therefore, it is hypothesized that the high pore pressure induced by the water injection in salt mine area should be partly responsible for the low friction coefficient. However, it is worthy to note that it is limited to discuss around the pore pressure change solely based on the CFS change. In addition, to conduct further quantitative analysis of the relationship between the pore pressure change due to the water injection in salt mine and the 2019 Changning earthquake, it is necessary to collect the detailed water injection and geology data, and to construct fined flow model in porous medium in salt mine area in the future study.

In addition, it is worthy of noting that the CFS due to the main shock is an important triggering factor in the occurrence of the aftershocks, however, the background stress due to tectonic motion, dynamic CFS caused by the coseismic fault rupture, anthropogenic activities (including the high-pressure water injection in the salt

mining area and the hydraulic fracturing in the oil exploration and production area) and other unknown factors could also contribute to the occurrence of the aftershocks of Changning earthquakes (Freed 2005). And a better insight of the relation between the triggering of the aftershocks and above-mentioned factors needs further comprehensive study in the future.

5 CONCLUSIONS

In this study, ALOS-2 and Sentinel-1 SAR images are firstly used to measure the coseismic surface deformation field of the 2019 M_s 6.0 Changning earthquake. Both the ascending and descending track ALOS-2 interferograms maintained the interfermetric coherence in the near- and far-fields of the seismogenic fault, but the Sentinel-1 interferograms lost the correlation in the near-field. The four tracks InSAR data are jointly used to estimate the faulting model of the 2019 Changning earthquake. The best-fitting result shows that a major fault plane dipping to southwest and a small backthrust fault dipping to northeast developing in Changning anticline are responsible for the 2019 Changning earthquake. The aftershocks and the CFS change distribution suggest the possibility that the aftershocks may have different motion patterns from the main shock. In addition, the CFS change due to the two large earthquakes occurred in the hydraulic fracturing area shows that the previous two events may have insignificant impact on the initial rupture of the hypocentre. However, they are found to have a positive triggering effect on the fault rupture in the northwest of the seismogenic fault. In the final, the water injection in the salt mine area could have caused high pore pressure and low friction coefficient in the seismic zone. And the quantitative effect on the main shock due to the water injection in salt mine area needs more detailed studies.

ACKNOWLEDGEMENTS

We thanks the constructional comments from Editor Kosuke Heki and two anonymous reviewers to largely improve the manuscript. We benefit from fruitful discussions with Renqi Lu. Appreciation is also owed to Hsiu-Fang Lee and Xia Zhong, who helped us to prepare the figures. This research is supported by the Funds for Funds for Creative Research Groups of China (Grant No. 41521002) (Grant No. 41521002), the Applied Basic Research Program of Department of Science and Technology of Sichuan Province (Grant No. 2020YJ0116), the Open Funding Project of State Key Laboratory of Geohazard Prevention and Geoenvironment Protection (Grant No. SKLGP2020K019), the National Key Research and Development Program of China (Grant Nos. 2018YFC1505402, 2018YFC1504901) and the National Natural Science Foundation of China (Grant Nos. 41472255, 41704014 and 41631073). The ALOS-2 SAR images were provided by the Japan Aerospace Exploration Agency (JAXA) under the ALOS-2 RA6 Project (PI No. 3255 and No. 3105).

REFERENCES

Bachmann, C.E., Wiemer, S., Goertz-Allmann, B.P. & Woessner, J., 2012. Influence of pore-pressure on the event-size distribution of induced earthquakes, *Geophys. Res. Lett.,* **39**(9), L09302, doi:10.1029/2012GL051480.

Cattin, R., Briole, P., Lyon-Caen, H., Bernard, P. & Pinettes, P., 1999. Effects of superficial layers on coseismic displacements for a dip-slip fault and geophysical implications, *Geophys. J. Int.,* **137**(1), 149–158.

Chen, C.W. & Zebker, H.A., 2002. Phase unwrapping for large SAR interferograms: statistical segmentation and generalized network models, *IEEE Trans. Geosci. Remote Sens.,* **40**(8), 1709–1719.

Ellsworth, W.L., 2013. Injection-induced earthquakes, *Science,* **341**(6142), 1225942, doi:10.1126/science.1225942.

Ellsworth, W.L., Llenos, A.L., McGarr, A.F., Michael, A.J., Rubinstein, J.L., Mueller, C.S., Petersen, M.D. & Calais, E., 2015. Increasing seismicity in the U. S. midcontinent: Implications for earthquake hazard, *Leading Edge,* **34,** 618–626.

Evans, K.F., Zappone, A., Kraft, T., Deichmann, N. & Moia, F., 2012. A survey of the induced seismic responses to fluid injection in geothermal and CO_2 reservoirs in Europe, *Geothermics,* **41,** 30–54.

Farahbod, A.M., Kao, H., Cassidy, J.F. & Walker, D., 2015. How did hydraulic-fracturing operations in the Horn River Basin change seismicity patterns in northeastern British Columbia, Canada? *Leading Edge,* **34**(6), 658–663.

Farr, T.G. *et al.*, 2007. The shuttle radar topography mission, *Rev. Geophys.,* **45**(2), 1–33.

Freed, A.M., 2005. Earthquake triggering by static, dynamic, and postseismic stress transfer, *Annu. Rev. Earth Planet. Sci.,* **33,** 335–367.

Gan, W., Zhang, P., Shen, Z.-K., Niu, Z., Wang, M., Wan, Y., Zhou, D. & Cheng, J., 2007. Present-day crustal motion within the Tibetan Plateau inferred from GPS measurements, *J. geophys. Res.,* **112**(B8), B08416, doi:10.1029/2005JB004120.

He, D., Lu, R., Huang, H., Wang, X., Jiang, H. & Zhang, W., 2019. Tectonic and geological background of the earthquake hazards in Changning shale gas development zone, *Petrol. Explor. Dev.,* **46**(3), 1–14, (in Chinese).

Hanssen, R.F., 2001. *Radar Interferometry: Data Interpretation and Error Analysis,* Kluwer.

Hsu, Y.-J., Rivera, L, Wu, Y.-M., Chang, C.-H. & Kanamori, H., 2010. Spatial heterogeneity of tectonic stress and friction in the crust: new evidence from earthquake focal mechanisms in Taiwan, *Geophys J. Int.,* **182**(1), 329–342.

Huang, M.-H., Tung, H., Fielding, E., Huang, H.-H., Liang, C., Huang, C. & Hu, J.-C., 2016. Multiple fault slip triggered above the 2016 Mw 6.4 MeiNong earthquake in Taiwan, *Geophys. Res. Lett.,* **43,** 7459–7467.

Kato, A., Kurashimo, E., Igarashi, T., Sakai, S. & Iidaka, T., 2009. Reactivation of ancient rift systems triggers devastating intraplate earthquakes, *Geophys. Res. Lett.,* **26,** L05301, doi:10.1029/2008GL036450.

Leonard, M., 2010. Earthquake fault scaling: self-consistent relating of rupture length, width, average displacement, and moment release. *Bull. seism. Soc. Am.,* **100**(5A), 1971–1988.

Le Béon, M. *et al.*, 2017. Shallow geological structures triggered during the Mw 6.4 Meinong earthquake, southwestern Taiwan, *Terr. Atmos. Ocean. Sci.,* **28**(5), 663–681.

Lei, X., Ma, S., Chen, W., Pang, C., Zeng, J. & Jiang, B., 2013. A detailed view of the injection-induced seismicity in a natural gas reservoir in Zigong, southwestern Sichuan Basin, China, *J. geophys. Res.,* **118,** 4296–4311.

Lei, X., Huang, D., Su, J., Jiang, G., Wang, X., Wang, H., Guo, X. & Fu, H., 2017. Fault reactivation and earthquakes with magnitudes of up to Mw4.7induced by shale-gas hydraulic fracturing in Sichuan Basin, *China, Sci. Rep.,* **7,** 7971, doi:10.1038/s41598-017-08557-y.

Lei, X., Wang, Z. & Su, J., 2019a. The December 2018 ML 5.7 and January 2019 ML 5.3 earthquakes in South Sichuan Basin induced by shale gas hydraulic fracturing, *Seismol. Res. Lett.,* **90**(3), 1099–1110.

Lei, X., Wang, Z. & Su, J., 2019b. Possible link between long-term and short-term water injections and earthquakes in salt mine and shale gas site in Changning, south Sichuan Basin, China, *Earth Planet. Phys.,* **3,** 510–525.

Liu, J.-Q. & Zahradnik, J., 2019. The 2019 MW 5.7 Changning earthquake, Sichuan Basin, China - a shallow doublet with different faulting styles, *Geophys. Res. Lett.,* **47**(4), e2019GL085408, doi:10.1029/2019GL085408.

Mahani, A.B., Schultz, R., Kao, H., Walker, D., Johnson, J. & Salas, C., 2017. Fluid injection and seismic activity in the northern Montney Play, British Columbia, Canada, with special reference to the 17 August 2015 Mw 4.6 induced earthquake, *Bull. seism. Soc. Am.,* **107,** 542–552.

McQuarrie, N., 2004. Crustal scale geometry of the Zagros fold–thrust belt, Iran, *J. Struct. Geol.,* **26**(3), 519–535.
Meng, L., McGarr, A., Zhou, L. & Zang, Y., 2019. An investigation of seismicity induced by hydraulic fracturing in the Sichuan Basin of China based on data from a temporary seismic network, *Bull. seism. Soc. Am.,* **109**(1), 348–357.
Nishimura, T., Tobita, M., Yarai, H., Amagai, T., Fujiwara, M., Une, H. & Koarai, M., 2008. Episodic growth of fault-related fold in northern Japan observed by SAR interferometry, *Geophys. Res. Lett.,* **35**(13), L13301, doi:10.1029/2008GL034337.
Okada, Y., 1985. Surface deformation to shear and tensile fault in a half-space, *Bull. seism. Soc. Am.,* **75**(4), 1135–1154.
Okada, Y., 1992. Internal deformation due to shear and tensile faults in a half-space, *Bull. seism. Soc. Am.,* **82**(2), 1018–1040.
Ruan, X., Cheng, W.Z., Zhang, Y.J. *et al.*, 2008. Research of the earthquakes induced by water injections in salt mines in Changning, Sichuan, *Earthq. Res. China,* **24**(3), 226–234, (in Chinese).
Rubinstein, J.L. & Mahani, A.B., 2015. Myths and facts on wastewater injection, hydraulic fracturing, enhanced oil recovery, and induced seismicity, *Seismol. Res. Lett.,* **86,** 1060–1067.
Rutqvist, J., Rinaldi, A.P., Cappa, F. & Moridis, G.J., 2015. Modeling of fault activation and seismicity by injection directly into a fault zone associated with hydraulic fracturing of shale-gas reservoirs, *J. Petrol. Sci. Eng.,* **127,** 377–386.
Sun, X., Yang, P. & Zhang, Z., 2017. A study of earthquakes induced by water injection in the Changning salt mine area, SW China, *J. Asian Earth Sci.,* **136,** 102–109.
Toda, S., Stein, R.S., Beroza, G.C. & Marsan, D., 2012. Aftershocks halted by static stress shadows, *Nat. Geosci.,* **5**(6), 410–413.
United States Geological Survey (USGS), 2019. M 5.8 - 19km S of Changning, China, https://earthquake.usgs.gov/earthquakes/eventpage/us600041ry/moment-tensor.
Walsh, F.R. & Zoback, M.D., 2015. Oklahoma's recent earthquakes and saltwater disposal, *Sci. Adv.,* **1,** e1500195, doi:10.1126/sciadv.1500195.
Wegmuller, U. & Werner, C., 1997. Gamma SAR processor and ineterferometry software, in *Proceedings of 3rd ERS Symposium, Space Service Environment (Special Publications 414, ESA),* Vol. **III,** pp. 1687–1692.
Weston, J., Ferreira, A.M.G. & Funnning, G.J., 2012. Systematic comparisons of earthquake source models determined using InSAR and seismic data, *Tectonophysics,* **532,** 61–81.
Yang, Y.-H., Chen, Q., Xu, Q., Liu, G. & Hu, J.-C., 2018a. Source model and Coulomb stress change of the 2015 Mw 7.8 Gorkha earthquake determined from improved inversion of geodetic surface deformation observations, *J. Geod.,* **93,** 333–351.
Yang, Y.-H., Tsai, M.-C., Hu, J.-C., Aurelio, M.A., Hashimoto, M., Escudero, J.A.P., Su, Z. & Chen, Q., 2018b. Coseismic slip deficit of the 2017 Mw 6.5 Ormoc earthquake that occurred along a creeping segment and geothermal field of the Philippine Fault, *Geophys. Res. Lett.,* **45,** 2659–2668.
Yang, Y.-H. *et al.*, 2018c. Mid-crustal thrusting and vertical deformation partitioning constraint by 2017 Mw 7.3 Sarpol Zahab Earthquake in Zagros Mountain belt, Iran, *Seismol. Res. Lett.,* **89**(6), 2204–2213.
Yang, Y.-H., Hu, J.-C., Chen, Q., Wang, Z.-G. & Tsai, M.-C., 2019. A blind thrust and overlying folding earthquake of the 2016 Mw 6.0 Hutubi earthquake in the northern Tien Shan Mountain fault-and-thrust belts, China, *Bull. seism. Soc. Am.,* **109**(2), 770–779.
Yi, G.X., Long, F., Liang, M.J. *et al.*, 2019. Focal mechanism solutions and seismogenic structure of the 17 June 2019 Ms 6.0 Sichuan Changning earthquake sequence, *Chinese J. Geophys.,* **62**(9), 3432–3447, (in Chinese).
Yue, L.-F., Suppe, J. & Hung, J.-H., 2005. Structural geology of a classic thrust belt earthquake: the 1999 Chi-Chi earthquake Taiwan (Mw = 7.6), *J. Struct. Geol.,* **27**(11), 2058–2083.
Zhu, H. & He, C., 2014. Focal mechanism Changning character of earthquake sequence induced by water injection: a case study of Changning sequence, Sichuan Province, *Earth Sci.-J. China Univ. Geosci.,* **39**(12), 1776–1782, (in Chinese).

SUPPORTING INFORMATION

Supplementary data are available at *GJI* online.

Figure S1. Estimated coseismic slip distribution on three-segment curved faulting model of the 2019 Changning earthquake.
Figure S2. Predicted InSAR deformation based on the estimated curved faulting model (Fig. S1) of the 2019 Changning earthquake.
Figure S3. The estimated faulting model with a dip angle of 50° of the 2019 Changning earthquake.
Figure S4. Predicted InSAR deformation based on the estimated faulting model with a dip angle of 50° (Fig. S3) of the 2019 Changning earthquake.
Figure S5. Checkboard test of the slip inversion of the 2019 Changning earthquake.
Figure S6. Coulomb failure stress change on the F2 due to the main fault rupture.
Figure S7. Distribution of the background seismicity, aftershocks and the coseismic faulting model.
Figure S8. Coulomb failure stress change at aftershocks cluster depth of 2 km with different receiver fault parameters caused by our preferred faulting model (Fig. 4) of the 2019 Changning earthquake.
Figure S9. Coulomb failure stress change at aftershocks cluster depth of 4 km with different receiver fault parameters caused by our preferred faulting model (Fig. 4) of the 2019 Changning earthquake.
Figure S10. Coulomb failure stress change at aftershocks cluster depth of 2 km with different rake angles caused by the faulting model with a dip angle of 50° (Fig. S3).
Figure S11. Coulomb failure stress change at aftershocks cluster depth of 4 km with different rake angles caused by the faulting model with a dip angle of 50° (Fig. S3).
Table S1. Parameters of the used radar interferometric pairs in this study.
Table S2. Focal mechanism solutions of the two large earthquakes that occurred in the hydraulic fracturing area.

Please note: Oxford University Press is not responsible for the content or functionality of any supporting materials supplied by the authors. Any queries (other than missing material) should be directed to the corresponding author for the paper.